



Nanostructured ZnO thin films prepared by sol–gel spin-coating

E. Heredia ^{a,*}, C. Bojorge ^a, J. Casanova ^a, H. Cánepa ^a, A. Craievich ^b, G. Kellermann ^c

^a UNIDEF (CONICET-MINDEF), J.B. de La Salle 4397, 1603 Villa Martelli, Pcia. de Buenos Aires, Argentina

^b Instituto de Física, Universidade de São Paulo, Cidade Universitária, 66318 São Paulo, SP, Brazil

^c Universidade Federal do Paraná, 19044 Paraná, Brazil



ARTICLE INFO

Article history:

Received 7 May 2014

Received in revised form 10 July 2014

Accepted 9 August 2014

Available online 19 August 2014

Keywords:

ZnO

Nanostructured thin films

XR

AFM

FESEM

GISAXS

ABSTRACT

ZnO thin films deposited on silica flat plates were prepared by spin-coating and studied by applying several techniques for structural characterization. The films were prepared by depositing different numbers of layers, each deposition being followed by a thermal treatment at 200 °C to dry and consolidate the successive layers. After depositing all layers, a final thermal treatment at 450 °C during 3 h was also applied in order to eliminate organic components and to promote the crystallization of the thin films. The total thickness of the multilayered films – ranging from 40 nm up to 150 nm – was determined by AFM and FESEM. The analysis by GIXD showed that the thin films are composed of ZnO crystallites with an average diameter of 25 nm circa. XR results demonstrated that the thin films also exhibit a large volume fraction of nanoporosity, typically 30–40 vol.% in thin films having thicknesses larger than ~70 nm. GISAXS measurements showed that the experimental scattering intensity is well described by a structural model composed of nanopores with shape of oblate spheroids, height/diameter aspect ratio within the 0.8–0.9 range and average diameter along the sample surface plane in the 5–7 nm range.

© 2014 Elsevier B.V. All rights reserved.

1. Introduction

Nanocrystalline ZnO is a material of great practical relevance because of its potential applications to the development of new gas and humidity sensors [1–3], UV detectors, optoelectronic devices [3,4], nanogenerators [5], etc. In addition, the porosity developed in ZnO thin films obtained by sol–gel favors other useful applications as substrates for catalysis, electrodes for solar cells, and for sensing of guest structures and biocompatible organic components.

The application to the development of conductive gas sensors composed of thin films of n-type zinc oxide is based on the dependence of the electrical characteristics of this material on the nature of the surrounding gas atmosphere. The performance of ZnO thin films as gas sensor depends on the internal microstructure of the material and on its surface geometry [6]. Thus, when this material is used as a gas sensor, a synthesis process leading to a controlled porous microstructure should be selected. Since the sensing process involves chemisorption, i.e. exchange of charges between adsorbed gaseous species and the metal oxide surface – the detailed characterization of the nanoporous structure of the materials is needed for adequate design of new sensor devices [6].

In a previous work, ZnO nanostructured films were obtained by the sol–gel technique [7], in this case drying the sample at room temperature after each deposit. The films prepared by this method are very porous, thin and flat, but their thicknesses are difficult to control.

In the present work, pure ZnO thin films were prepared by the sol–gel method and deposited by spin-coating. In this procedure the samples were submitted to successive heat treatments at 200 °C during 10 min after each deposit. This led to the consolidation of the different layers and to the proper control of the final film thickness.

The ZnO films were characterized by grazing-incidence X-ray diffraction (GIXD), atomic force microscopy (AFM), field emission scanning electron microscopy (FESEM), X-ray reflectivity (XR) and grazing-incidence small-angle X-ray scattering (GISAXS).

2. Experimental

2.1. Preparation of the thin films

Nanocrystalline pure zinc oxide films were obtained by sol–gel processing using a precursor solution composed of zinc acetate dihydrate dissolved in absolute ethanol, deionized water and acetic acid, as described in a previous work [7]. This solution was then deposited on amorphous SiO₂ flat substrates by applying several times the spin-coating technique during 10 s at 3000 rpm. In order

* Corresponding author. Tel.: +54 11 47098100x1212.

E-mail address: heredia.edu@gmail.com (E. Heredia).

to consolidate the deposited material after each deposition, the samples were subjected to partial heat-treatments during 10 min at 200 °C. This procedure led to the formation of thin films composed of 2, 4, 6 and 8 layers. Finally, the multilayered films were annealed during 3 h at 450 °C in order to achieve their whole crystallization and to eliminate organic residues.

2.2. Characterization techniques

The samples were studied by GIXD, by using a PW 3710 Philips diffractometer with Cu K α radiation (wavelength $\lambda = 1.542 \text{ \AA}$), at a constant grazing incidence angle $\alpha_i = 1^\circ$. The analysis of the GIXD patterns indicated that the thin films are crystalline, all the observed Bragg peaks corresponding to ZnO-wurtzite crystals. The average crystallite sizes, D , were determined from (100) and (101) peaks – the two most intense reflections – by applying Scherrer equation, $D = 0.9\lambda/(B \cos\theta_B)$, where B is the integral breadth (in radians) and θ_B the Bragg angle of the diffraction peak [8].

By applying the AFM technique, the root-mean-square surface roughness parameter, η_{AFM} , and the film thickness, t_{AFM} , were determined. The thickness was measured by determining the magnitude of the edge produced by scratching the thin films with a steel cutting tool. The AFM images were processed with the WSxM free software [9]. The thicknesses of the films were also determined from FESEM images of the cross-section perpendicular to the film surface.

XR and GISAXS experiments were performed using the D10A-XRD2 beam line of the LNLS synchrotron radiation facility, Campinas, Brazil, using a monochromatic 8 keV ($\lambda = 1.549 \text{ \AA}$) photon beam.

XR measurements were carried out using $\alpha - 2\alpha$ scans, by varying the α grazing incidence angle between 0.1° and 2°. In general, X-ray reflectivity patterns allow for determining the average density, the thickness and the roughness of the films by fitting a structure model to the experimental XR curve [10–12]. Since the XR patterns did not exhibit well-defined Kiessig fringes [13] the thickness could not be determined. Thus we have derived the average film densities from the values of the critical angle of total X-ray reflection.

The GISAXS technique was applied to determine the shape and the size distribution of pores in the nanometric scale embedded in the thin films. A KODAK imaging-plate was used to record the 2D GISAXS patterns. The grazing incidence angle of the X-ray beam was set at $\alpha_i = 0.4^\circ$, slightly above the critical angle for total reflection of bulk ZnO ($\alpha_c = 0.33^\circ$), for all the studied samples. The analysis of the GISAXS intensity was performed using the lsGisaxs 2.6 program [14].

3. Results

3.1. Grazing incidence X-ray diffraction

The GIXD patterns of the ZnO thin films deposited on silica glass Plates in the 2θ range between 30° and 39° – are plotted in Fig. 1. In order to compare the crystallographic parameters related to the crystalline structure of the different studied thin films, the GIXD patterns were determined by using identical experimental conditions. The angular positions of the Bragg peaks in the diffraction curves – (100), (002) and (101) reflections – are in agreement with those of the expected peaks for ZnO crystallites with wurtzite-like structure. These peaks are superposed to the diffuse scattering halo produced by the amorphous silica glass substrate.

The inset in Fig. 1 shows the added areas (Σ) of the three main peaks of ZnO. The added areas versus number of layers (n), $\Sigma \times n$ plots, indicate an approximately linear behavior. As the X-ray

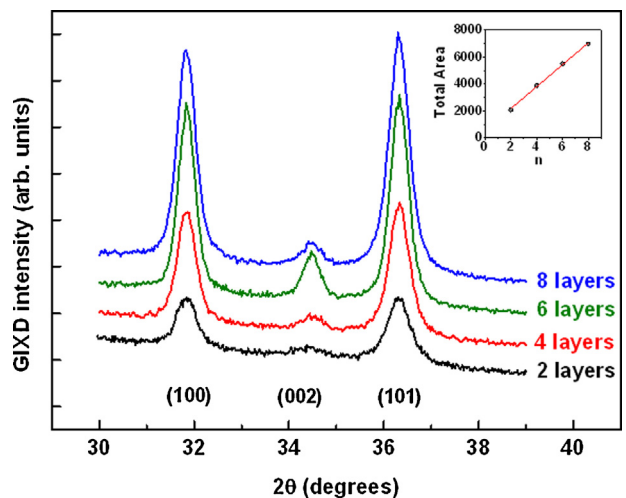


Fig. 1. GIXD diagrams of ZnO films carried out using Cu K α radiation in grazing-incidence geometry (grazing incidence angle $\theta = 1^\circ$). Inset: area of the diffraction peaks ($\Sigma = A_{(100)} + A_{(002)} + A_{(101)}$) versus the number of deposits, n .

absorption of the thin films here studied is weak, Σ is roughly proportional to the irradiated ZnO mass. Therefore, the behavior in the $\Sigma \times n$ curve in Fig. 1 indicates that nearly the same mass of ZnO is deposited in each layer.

The values of the average diameters of the ZnO crystallites D corresponding to the studied films, determined from the integral breadth of the main Bragg peaks after correction for instrumental broadening, are reported in Table 1.

3.2. Atomic force microscopy and field emission scanning electron microscopy

The morphology of the surface of the thin films can be seen in the AFM images shown in Fig. 2. In the upper left corner of all the images shown in Fig. 2 the distributions of the heights normal to the film surfaces are plotted. The root mean square parameters, η_{AFM} , were determined from these histograms using the WSxM software [9]. The results reported in Table 1 indicate that the magnitude of the roughness increases for increasing number of deposited layers, all values being within the 5–10 nm range. In the bottom right corner of each image in Fig. 2, we have plotted the profiles derived from AFM images corresponding to the thin film area after scratching it with a steel cutting tool. The thicknesses of the thin films determined by measuring the step depth of the grooves, t_{AFM} , are reported in Table 1, their values ranging from 43 to 147 nm.

Fig. 3 depicts the FESEM micrographs of the cross-section perpendicular to the ZnO thin film surfaces. In each image the regions corresponding to the film and substrate are clearly apparent. The thicknesses of the films, t_{FESEM} , obtained by 4, 6, and 8 successive spin-coating depositions are reported in Table 1. The thickness of the thinnest (2-layers) film could not be measured by FESEM because the image was blurry, this being probably due to a damaging of the thin film cross-section produced during the cutting process. The values of the thicknesses derived from FESEM measurements, t_{FESEM} , increase for increasing number of deposited layers, in good agreement with the observed trend of the thickness determined by AFM.

3.3. X-ray reflectivity

The XR patterns corresponding to samples with different numbers of ZnO deposited layers are plotted in Fig. 4. The reflectivity

Table 1

Parameters obtained from the films with different numbers of deposited layers (n) characterized by different techniques (GIXD, AFM, FESEM and GISAXS). D is the average ZnO crystallite diameter, t the film thickness, η the RMS surface roughness, v the height/width aspect ratio, $\langle R \rangle$ the average pore radius in the film plane direction and σ_R the size dispersion (standard deviation) of the nanopores radius.

n	GIXD	FESEM	AFM	GISAXS			
	D (nm)	t (nm)	t (nm)	η (nm)	v	$\langle R \rangle$ (nm)	σ_R (nm)
2	20	—	43	5.6	0.88	4.98	2.20
4	23	86	77	5.3	0.80	6.88	2.65
6	28	107	103	6.9	0.83	6.60	2.50
8	23	146	147	10.2	0.88	6.10	1.97

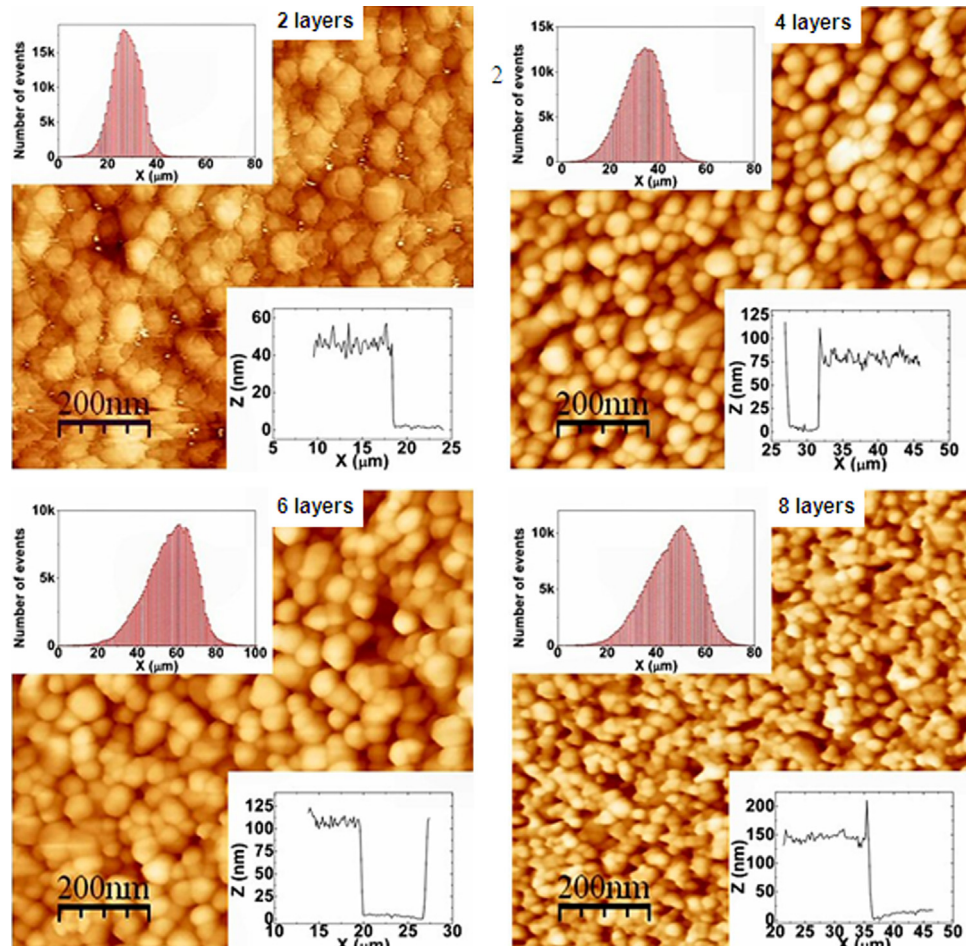


Fig. 2. AFM micrographs of the thin films with 2, 4, 6 and 8 deposited ZnO layers. For each image the height distribution function and the AFM profile showing the height step of the film scratched with a steel cutting tool are exhibited in the upper left corner and in the bottom right corner respectively.

curves were corrected in order to take into account that, at very small grazing incidence angles, only a fraction of the total incident X-ray beam is intercepted by the sample surface [13,15].

Usually, oscillations in X-ray reflectivity curves (Kiessig fringes) – generated by the interference of the reflected beams at the air/film

and film/substrate interfaces – are observed above the critical angle for total reflection α_c for a thin film having constant thickness deposited on a flat thick substrate. In this case, from the period of the oscillations, the thickness of thin film can be determined [13]. However, for the curves shown in Fig. 4 the oscillation are very

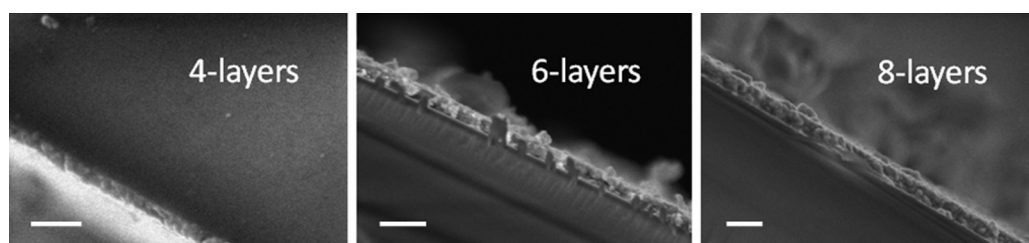


Fig. 3. FESEM micrographs of the ZnO/silica cross-section corresponding to the number of layers indicated in each image. Bars in each micrograph correspond to 300 nm.

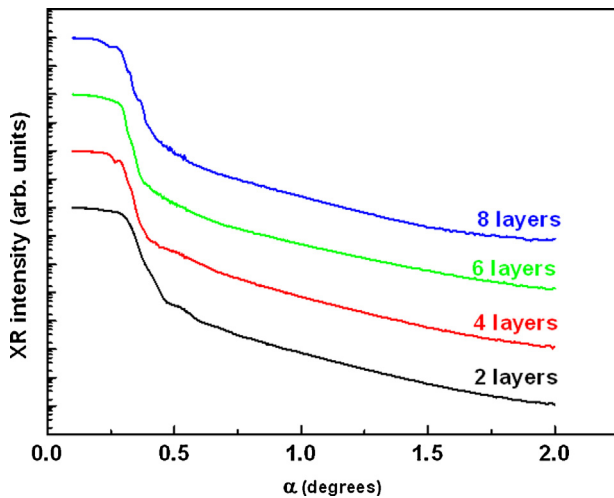


Fig. 4. X-ray reflectivity curves corresponding to the thin films with 2, 4, 6 and 8 ZnO layers. The curves in the figure are vertically shifted for clarity.

much damped and thus precise determinations of the thicknesses of the thin films were not achieved.

However, for each curve the X-ray critical angle of total reflection α_c – defined as the angle for which the reflectivity (ratio between the power of the reflected and incidence beam) is equal to 0.5 – was determined. From the α_c values the specific mass ρ of the thin films were calculated by using the relation [13]:

$$\rho = \frac{\pi}{\lambda^2 r_e N_a} \cdot \frac{A}{Z + f'} \cdot \alpha_c^2 \quad (1)$$

where λ is the X-ray wavelength, r_e the classical electron radius, N_a the Avogadro number, Z , A and f' are the average values of the atomic number, the atomic mass and the real part of the anomalous part of the atomic scattering factor, respectively.

The average mass densities of the studied thin films, ρ , were determined by using Eq. (1) and reported in Table 2. The mass densities of all the studied thin films are lower than the density of bulk ZnO, i.e. $\rho_{\text{ZnO}} = 5.61 \text{ g/cm}^3$. We have assigned the low values measured for the mass densities – ranging from 3.62 up to 4.71 g/cm^3 – to the presence of nanopores coexisting with ZnO nanocrystals with the expected density for bulk crystals. Thus the volume fraction of the porosity, p , was determined as [7]:

$$p = 1 - \frac{\rho}{\rho_{\text{ZnO}}} \quad (2)$$

The values of the volume fraction of nanopores determined by applying Eq. (2) are within the 0.16 and 0.36 range. The volume fraction of porosity in the 2-layers film is noticeably lower than that of thicker films. However a not well-defined trend in the dependence of this parameter on the number of deposited layers is apparent from our data.

3.4. Grazing incidence small-angle scattering

3.4.1. Geometry and preliminary analysis

Fig. 5 displays the geometry of the setup used in the study of ZnO thin films by GISAXS. The scattering intensity was measured as a function of the scattering vector given by [14]:

$$\bar{q} = \vec{k}_f - \vec{k}_i = \frac{2\pi}{\lambda} \begin{pmatrix} \cos 2\theta \cos \alpha_f - \cos \alpha_i \\ \sin 2\theta \cos \alpha_f \\ \sin \alpha_f + \sin \alpha_i \end{pmatrix} \quad (3)$$

where \vec{k}_i and \vec{k}_f are the wave-vectors of the incoming and scattered beams, respectively, $\lambda = 1.549 \text{ \AA}$ is the wavelength of the incidence

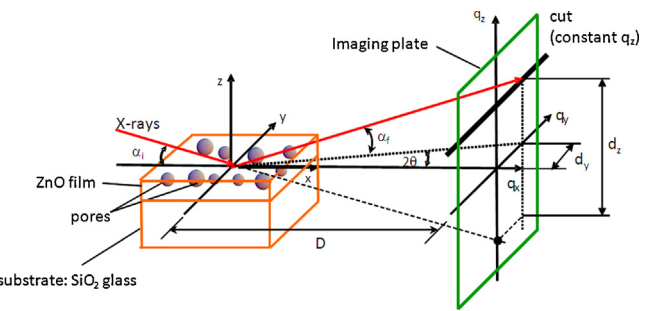


Fig. 5. Geometry of the setup used in the study of the ZnO thin films by GISAXS.

X-rays, 2θ the horizontal scattering angle, α_i the grazing incidence angle and α_f the exit angle between the scattered beam and the sample surface [16–18].

The 2D GISAXS intensity patterns corresponding to the films having 2 and 4 layers are displayed in Fig. 6. The vertical strip in the center of scattering patters is the shadow of the beam-stopper used to stop the incident and totally reflected X-ray beams. We have assumed that the observed X-ray scattering intensity is produced by the contrast between the density of pores, with density $\rho_p = 0$, and that of the bulk ZnO, ρ_{ZnO} . The GISAXS pattern of a bare glass, i.e. without deposition of the ZnO film, not showed here, exhibit a weak and nearly constant intensity, except close to the shadow edges of the beam-stopper, where part of the reflected intensity is apparent. Before further analysis, the contribution to GISAXS intensity from the bare glass and also the parasitic scattering intensity produced by the Kapton windows, slits and air paths was also properly subtracted.

The maximum intensity at the bottom of the scattering pattern at $q_z = (2\pi/\lambda)(\sin \alpha_c + \sin \alpha_i)$ is due to the modulation of the pores scattering intensity by the Fresnel transmission function of the air/film interface. This maximum occurs at $\alpha_f = \alpha_c$, α_c being the critical angle for X-ray total external reflection at the interface. This gives rise to the so-called Yoneda peak in $I \times q_z$ profiles. The position of the Yoneda peak with respect to the sample surface depends only on the critical angle, being independent of the grazing incidence angle [13]. Consequently, the angle α_f at which the Yoneda peak appears in the GISAXS patterns can also be used to determine

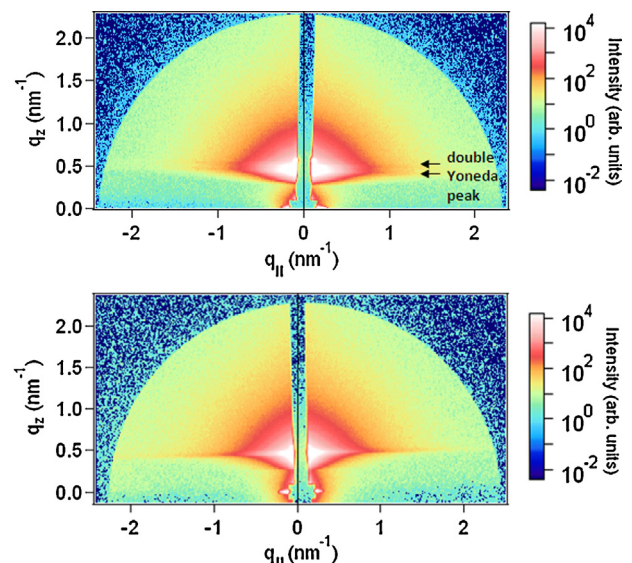


Fig. 6. 2D GISAXS intensity patterns of 2-layers (above) and 4-layers (below) thin films prepared by spin-coating technique. The sample with 2-layers shows an additional Yoneda peak attributed to the ZnO/SiO₂ interface.

Table 2

Critical angle (α_c), average mass density (ρ) and volume fraction of the nanoporosity (p) obtained by XR and GISAXS. The mass density derived from GISAXS data were determined by using two different procedures: (i) from the position of α_f of the Yoneda peak and (ii) from a best fitting procedure using IsGISAXS program to derive the real part of the film refraction index ($1 - \delta$). In the last procedure ρ and p were then determined by using Eqs. (1) and (2), respectively.

n	XR			GISAXS (Yoneda peak)			IsGISAXS	
	α_c (°)	ρ (g/cm ³)	p	α_c (°)	ρ (g/cm ³)	p	ρ (g/cm ³)	p
2	0.300	4.71	0.16	0.300	4.71	0.16	4.75	0.15
4	0.261	3.56	0.36	0.260	3.54	0.36	3.90	0.30
6	0.279	4.09	0.27	0.260	3.54	0.36	3.40	0.39
8	0.263	3.62	0.35	0.263	3.62	0.35	3.45	0.38

the critical angle and, thus, to calculate the film density by applying Eq. (1). The critical angles obtained from the GISAXS intensity patterns are reported in Table 2. These values are in good agreement with those determined from X-ray reflection measurements (Section 3.3).

An additional peak is observed at $\alpha_f = 0.22^\circ$ for the 2-layers ZnO film (Fig. 6 above). The α_f value of this peak coincides with the critical angle of the bare SiO₂ substrate and corresponds to the Yoneda peak due to the modulation of the Fresnel transmission function of the scattering of fluctuation in electron density of the glass substrate. The Yoneda peak due to the substrate is only observed when the film/air interface is very rough while the absorption of X-rays in the film is low, such as in the case of the 2-layers ZnO thin film. For thicker films the absorption of X-rays is higher and, in these cases, the second Yoneda peak vanishes.

3.4.2. Experimental results and modeling

Fig. 7 displays I versus $q_{||} = \sqrt{q_x^2 + q_y^2}$ GISAXS profiles (circles) corresponding to ten cuts performed in Fig. 6 below for a 4-layers film for the indicated q_z values. For clarity the curves were vertically displaced from the bottom to top by multiplying by increasing powers of 10. These GISAXS intensity profiles were analyzed using the IsGISAXS program by Lazzari [14]. In our case the GISAXS patterns were modeled assuming that the scattering intensity is produced by a polydisperse set of spatially uncorrelated pores embedded in the ZnO film, the pores having the shape of an ellipsoid of revolution and all the same high/width aspect ratio. The GISAXS intensity

$I(q_{||}, \alpha_i, \alpha_f)$ produced by a spatially uncorrelated set of ellipsoidal empty nanopores with same aspect ratio v , a size distribution given by $N(R)$, embedded in a layer deposited on a substrate, is written as [14]:

$$I(q_{||}, \alpha_i, \alpha_f) \propto \int N(R) \left| \Phi(q_{||}, k_z^i, k_z^f, R, v) \right|^2 dR, \quad (4)$$

where Φ is the effective scattering factor resulting from the coherent interference between four waves:

$$\begin{aligned} &= T_1(\alpha_i)T_1(\alpha_f) \exp[-i(\tilde{k}_z^f - \tilde{k}_z^i)\delta]F(q_{||}, \tilde{k}_z^f - \tilde{k}_z^i, R, v) \\ &+ R_1(\alpha_i)T_1(\alpha_f) \exp[-i(\tilde{k}_z^f + \tilde{k}_z^i)\delta]F(q_{||}, \tilde{k}_z^f + \tilde{k}_z^i, R, v) \\ &+ T_1(\alpha_i)R_1(\alpha_f) \exp[-i(-\tilde{k}_z^f - \tilde{k}_z^i)\delta]F(q_{||}, -\tilde{k}_z^f - \tilde{k}_z^i, R, v) \\ &+ R_1(\alpha_i)R_1(\alpha_f) \exp[-i(-\tilde{k}_z^f + \tilde{k}_z^i)\delta]F(q_{||}, -\tilde{k}_z^f + \tilde{k}_z^i, R, v) \end{aligned} \quad (5)$$

$R_1(\alpha_i, \alpha_f)$ and $T_1(\alpha_i, \alpha_f)$ being the amplitudes of the upwards and downwards propagating waves in the layer, \tilde{k}_z^i and \tilde{k}_z^f are the perpendicular components of the refracted and scattered wave-vectors inside the layer and δ the average buried depth of nanopores. F is the form factor associated to an ellipsoid of revolution. The $T_1(\alpha_f)$ function gives rise to above described Yoneda peak. The thickness obtained by AFM and the refractive index calculated from the Yoneda peak position were used as input data for fitting the ten curves of each diagram.

In our model the parameter R is the semi axis of the ellipsoid in the film plane, and H the axis of ellipsoid in the direction normal to this plane, the aspect ratio being so equal to $v = H/2R$. The best agreement between experimental and calculated curves was obtained when the lognormal function

$$N(R) = \frac{N}{\sqrt{2\pi}R \log(\sigma/R_0)} \cdot \exp \left[-\frac{1}{2} \left(\frac{\log(R/R_0)}{\log(\sigma/R_0)} \right)^2 \right] \quad (6)$$

was used to describe the size distribution function $N(R)$ of the pores.

Different GISAXS curves for the 4-layers film obtained by applying the best fitting procedure – using the IsGISAXS program – are plotted as solid lines in Fig. 7. The average radius (R) and the standard deviation, σ_R , of the radius distribution were determined from the parameters R_0 and σ of Eq. (6) [7]. Similar agreements between the experimental GISAXS results and the best fitted modeled curves were found for the other studied thin films. The values of $\langle R \rangle$, σ_R and v of the studied thin films are reported in Table 1.

3.4.3. Discussion of GISAXS results

The values reported in Table 1 indicate that the aspect ratio v of the different studied thin films ranges between 0.80 and 0.88. This result implies that in all the studied samples the nanopores are flattened in the direction normal to the film surface. This effect was already observed in a previous study by GISAXS of ZnO thin films

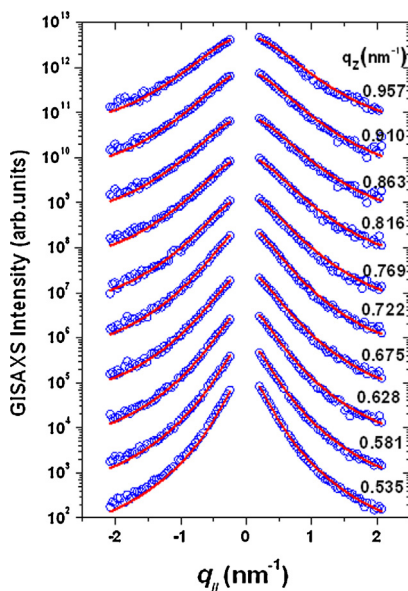


Fig. 7. GISAXS intensity profiles extracted from 2D GISAXS intensity patterns of 4-layers film (Fig. 6) at the indicated q_z values (circles) and best fitted curves (solid lines) calculated using the IsGISAXS program assuming the model described in the text. For clarity the curves were multiplied, from bottom to top, by increasing powers of ten.

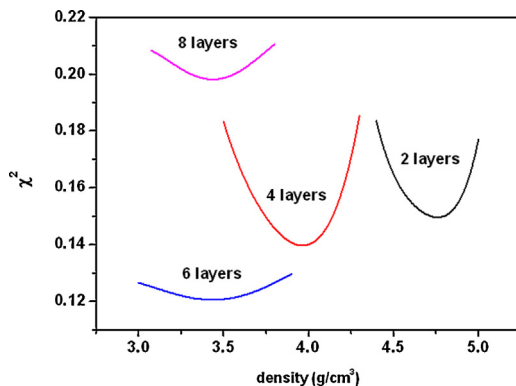


Fig. 8. Chi-square χ^2 factor related to the goodness of the fits using IsGISAXS program as a function of the specific mass for the thin films. The curves correspond to films having 2, 4, 6 and 8 ZnO layers.

prepared by a different deposition method and was attributed to the decrease in the film thickness as a consequence of their compaction during the final annealing of the samples [7].

The average lateral radius (R) of nanopores ranges from about 5 nm up to 7 nm without a clear trend for different number of deposited ZnO layers. The standard deviation in the nanopores radius does not significantly vary with the film thickness, the value of this parameters being maintained within the 2 nm to 2.7 nm range. GISAXS results (Table 1) do not show a clear relation between the morphology and size of nanopores (v , $\langle R \rangle$, and σ_R) and the number of deposited ZnO layers (n).

In addition to the modeling of the morphology and size of nanopores, the IsGISAXS program was also used to determine the real ($1 - \delta$) and the imaginary part (β) of the refraction index of the thin films resulting from the best agreement between experimental and fitted curves in the region of GISAXS intensity affected by the Fresnel transmission function, i.e. around the Yoneda peak. From the δ values obtained from this best fitting procedure and Eq. (1), the average mass density (specific mass) of the thin films were determined. Fig. 8 displays the dependence between the chi-square χ^2 factors – related to the goodness of the fits performed varying the input (δ and $\beta = 2.044E - 2\delta$) parameters – and the average mass density of the thin films. It was observed that for each sample there is a density value that minimizes the χ^2 vs. ρ function (Fig. 8). This value was taken as the most probable for the average density ρ .

The average thin film densities (determined from IsGISAXS program) and the respective volume fraction of porosity, p , calculated using Eq. (2), are also reported in Table 2. It can be seen that such values are in good agreement with those determined from XR and GISAXS (Yoneda peak) data.

In summary, the average density derived from GISAXS data were determined by two different procedures, namely: (i) the position of α_f of the Yoneda peak and (ii) a best fitting procedure using the IsGISAXS program to determine the real ($1 - \delta$) and the imaginary (β) parts of the film refraction index. From δ values, ρ and p parameters were calculated using Eqs. (1) and (2), respectively. These results confirm the presence of porosity in the ZnO films. The small differences in ρ (and so p) values determined by GISAXS and XR, can be attributed to uncertainties in the values of the critical angle, α_c , and differences in probed depth in XR and GISAXS experiments.

4. Conclusion

The structures of thin films composed of nanometric ZnO crystallites prepared by spin-coating and supported on a flat silica substrate were characterized by GIXD, AFM, FESEM, XR and GISAXS. Samples with 2, 4, 6 and 8 successive depositions were studied. All

samples were subjected to several thermal treatments at 200 °C for 10 min after each deposit and a final annealing at 450 °C during 3 h.

The different studied thin films consist of ZnO nanocrystals with wurtzite-like crystalline structure similar to the structure of bulk ZnO. The average nanocrystal sizes derived from GIXD range from 20 nm up to 28 nm. These sizes are somewhat larger than those reported in a previous investigation of samples subjected to equivalent thermal treatment but prepared by another procedure (dip-coating) [7].

The thicknesses of the ZnO thin films determined by AFM range from 43 nm for two layered up to 147 nm for eight layered films, these values being in good agreement with the thicknesses determined by FESEM. The root mean square surface roughness parameter determined by AFM imaging increases from 5.3 up to 10.2 nm for increasing number of the layers.

All the studied ZnO thin films exhibit a nanoporous structure. Our GISAXS characterization indicates the presence of nanopores with an ellipsoidal shape flattened along the direction normal to the thin film surface with aspect ratios $0.80 < v < 0.88$, the average lateral radius of pores (R) ranging from 5.0 nm up to 6.9 nm for 2-layers and 8-layers films, respectively.

As it can be verified in Table 2, the average density corresponding to the film with 2-layers ($n=2$) is clearly higher than those of thicker films. On the other hand, the thinnest film exhibit both roughness and average nanopore radius significantly lower than those of the thicker films (Table 1). These different features suggest an influence from the substrate surface that affects more the thinnest two layered film than the others thicker films.

Finally, our results indicate that the average size and morphology of nanopores and ZnO crystallites are essentially the same for all the studied thin films, except for the thinnest 2-layer film. This finding suggests that the ZnO thin films with four or more layers, prepared by the spin-coating process described here and irrespective of their final thickness, exhibit equivalent and reproducible structural features.

Acknowledgements

Authors are indebted to Silvio Ludueña and Claudia Marchi by their helping in AFM and FESEM techniques. We also want to express their gratefulness to UNIDEF (CONICET-MINDEF) (Argentina), CNPq (Brazil), PROSUL (Brazil), LNLS (Brazil) and YPF Foundation (Argentina), for the subsidies received for the realization of this work.

References

- [1] A. Erol, S. Okur, B. Comba, O. Mermel, M.C. Arıkan, Humidity sensing properties of ZnO nanoparticles synthesized by sol-gel process, *Sens. Actuators B-Chem.* 145 (2010) 174–180.
- [2] E. Broitman, C. Bojorge, F. Elhordoy, V. Kent, G. Zanini, Gadioli, R.E. Marotti, H. Cánepa, E.A. Dalchiele, Comparative study on the properties of ZnO nanowires and nanocrystalline thin films, *Surf. Coat. Technol.* 213 (2012) 59–64.
- [3] L. Schmidt-Mende, J.L. MacManus-Driscoll, ZnO-nanostructures, defects, and devices, *Mater. Today* 10 (5) (2007) 40–48.
- [4] Ü. Özgür, D. Hofstetter, H. Morkoç, ZnO devices and applications: a review of current status and future prospects, *Proc. IEEE* 98 (7) (2010) 1255–1268.
- [5] Z.L. Wang, The new field of nanopiezotronics: review, *Mater. Today* 10 (5) (2007) 20–28.
- [6] K. Hoydalsvik, T. Barnardo, R. Winter, S. Haas, D. Tatchev, A. Hoell, Yttria-zirconia coatings studied by grazing-incidence small-angle X ray scattering during in-situ heating, *Phys. Chem. Chem. Phys.* 12 (2010) 14492–14500.
- [7] J.R. Casanova, E.A. Heredia, C.D. Bojorge, H.R. Cánepa, G. Kellermann, A.F. Craievich, Structural characterization of supported nanocrystalline ZnO thin films prepared by dip-coating, *Appl. Surf. Sci.* 257 (2011) 10045–10051.
- [8] H.P. Klug, L.E. Alexander, *X-ray Diffraction Procedures for Polycrystalline and Amorphous Materials*, John Wiley & Sons, New York, 1974.
- [9] I. Horcas, R. Fernandez, J.M. Gomez-Rodriguez, J. Colchero, J. Gomez-Herrero, A.M. Baro, *Rev. Sci. Instrum.* 78 (2007) 013705–013708.

- [10] C. Braun, Parratt 32 Version 1.6 Software, Neutron Scattering Center, Hahn Maitner Institute, Berlin, 1999.
- [11] L.G. Parratt, Surface studies of solids by total reflection of X-rays, Phys. Rev. 95 (1954) 359–369.
- [12] L. Nevot, P. Croce, Caractérisation des surfaces par réflexion rasante de rayons X. Application à l'étude du polissage de quelques verres silicates, Rev. Phys. Appl. 15 (1980) 761–779.
- [13] M. Tolan, X-ray Scattering from Soft-matter Thin Films, Springer, Berlin Heidelberg/New York, 1999.
- [14] R. Lazzari, J. Appl. Crystallogr. 35 (2002) 406–421.
- [15] A. Gibaud, G. Vignaud, S.K. Sinha, The correction of the geometrical factor in the analysis of X-ray reflectivity, Acta Crystallogr. A 49 (1993) 642–648.
- [16] R. Lazzari, IsGISAXS Software Version 2.6, Institut des NanoSciences de Paris, Universités Pierre et Marie Curie et Denis Diderot, CNRS, Paris, France, 2006.
- [17] S.K. Sinha, E.B. Sirota, S. Garoff, H.B. Stanley, X-ray and neutron scattering from rough surfaces, Phys. Rev. B 38 (1988) 2297–2311.
- [18] M. Rauscher, T. Salditt, H. Spohn, Small-angle X-ray scattering under grazing incidence: the cross section in the distorted-wave Born approximation, Phys. Rev. B 52 (1995) 16855–16863.